Fourier magnetic imaging with nanoscale resolution and compressed sensing speed-up using electronic spins in diamond

K. Arai[1‡], C. Belthangady[2,3‡], H. Zhang[2,3‡], N. Bar-Gill[2,3†], S. J. DeVience[4], P. Cappellaro[5], A. Yacoby[3] and R. L. Walsworth[2,3,6★]

Optically detected magnetic resonance using nitrogen–vacancy (NV) colour centres in diamond is a leading modality for nanoscale magnetic field imaging[1-3], as it provides single electron spin sensitivity[4], three-dimensional resolution better than 1 nm (ref. 5) and applicability to a wide range of physical[6-13] and biological[14,15] samples under ambient conditions. To date, however, NV-diamond magnetic imaging has been performed using 'real-space' techniques, which are either limited by optical diffraction to ~250 nm resolution[16] or require slow, point-by-point scanning for nanoscale resolution, for example, using an atomic force microscope[17], magnetic tip[5], or super-resolution optical imaging[18,19]. Here, we introduce an alternative technique of Fourier magnetic imaging using NV-diamond. In analogy with conventional magnetic resonance imaging (MRI), we employ pulsed magnetic field gradients to phase-encode spatial information on NV electronic spins in wavenumber or 'k-space'[20] followed by a fast Fourier transform to yield real-space images with nanoscale resolution, wide field of view and compressed sensing speed-up.

The key advantages of NV-diamond Fourier magnetic imaging, relative to real-space imaging, are (1) spatially multiplexed detection[21,22], which enhances the signal-to-noise ratio (SNR) for typical NV centre densities, (2) a high data acquisition rate that can be further boosted with compressed sensing[23,24], and (3) simultaneous acquisition of signal from all NV centres in the field of view (FOV), which allows temporally correlated dynamics to be probed and provides isolation from system drift. Importantly, our technique achieves Fourier magnetic imaging via phase-encoding of the detector (the NV spins in diamond), which is more widely applicable to the diversity of nanoscale magnetic phenomena in condensed matter systems than existing Fourier magnetic imaging techniques, which perform phase-encoding on spins in the sample, for example, protons in organic solids[22]. As described in the following, we demonstrate one-dimensional imaging of individual NV centres with <5 nm resolution, two-dimensional imaging of multiple NV centres with ~30 nm resolution, and two-dimensional imaging of nanoscale magnetic field patterns with a magnetic gradient sensitivity of ~14 nT nm^{-1} Hz$^{-1/2}$ and spatial dynamic range (FOV/resolution) of ~500. We also show that compressed sensing can accelerate the image acquisition time by an order of magnitude.

Schematic views of the Fourier magnetic microscope are presented in Fig. 1a,b. The diamond sample has a thin layer of NV centres at the surface, created by ion implantation (see Methods). NV electronic spin states (Fig. 1c) are optically polarized with green illumination, coherently manipulated using resonant microwave fields applied by a microwave loop, and detected via spin-state-dependent fluorescence measurements. Strong, uniform magnetic field gradients for NV spin phase-encoding are generated by currents sent though pairs of gold wires (gradient microcoils). As a demonstration, another current sent through an external-field wire produces a non-uniform magnetic field pattern that can be imaged with the NV sensors in the sample. Figure 1b shows a simulation of the gradient produced by a current of 1 A sent through the gradient microcoils. At the centre of the microcoils, the gradient magnitude projected onto the NV quantization axis ζ is $|dB_\zeta/dx| = |dB_\zeta/dy| \approx 0.7$ G μm^{-1} and varies by <1% over a 15×15 μm^2 region.

The Fourier magnetic imaging pulse sequence consists of a laser initialization pulse, microwave dynamical-decoupling pulses for spin-state manipulation[25,26] and a laser readout pulse (Fig. 1d). A pulsed gradient field (dB_ζ/dx and/or dB_ζ/dy) for NV spin phase-encoding is applied during the microwave sequence. The sign of the gradient is switched during alternate free precession intervals to enable a.c. magnetic field sensing. The NV spin at position $\mathbf{r}_0$ thus acquires a position-dependent phase $\varphi = 2\pi\mathbf{k} \cdot \mathbf{r}_0$, where $\mathbf{k} = (2\pi)^{-1}\gamma\tau(dB_\zeta/dx, dB_\zeta/dy)$ defines the imaged point in the two-dimensional Fourier or k-space. Here, $\gamma/2\pi = 2.8$ MHz G^{-1} is the NV gyromagnetic ratio and τ is the total precession time. The optical NV signal for this k-space point is proportional to the cosine of the acquired phase φ: $s(\mathbf{k}) \sim \cos(2\pi\mathbf{k} \cdot \mathbf{r}_0)$. By incrementally stepping through a range of amplitudes for the applied magnetic field gradient, while keeping τ fixed, the NV signal is measured as a function of $\mathbf{k}$ to produce a k-space image. The real-space image is then reconstructed by Fourier transformation of the k-space image; that is, $S(\mathbf{r}) = F[s(\mathbf{k})]$, where abs$[S(\mathbf{r})]$ gives the positions of the NV centres. The pixel resolution of the real-space image is $(2k_{max})^{-1}$, where $k_{max} = (2\pi)^{-1}\gamma\tau(|dB_\zeta/dx|, |dB_\zeta/dy|)_{max}$ is the maximum k value used in the measurement.

As a first demonstration of NV Fourier imaging, we acquired a one-dimensional image of a single NV centre in a sample with low NV density (sample A, see Methods) by varying only the dB_ζ/dx gradient strength and using a four-pulse Carr–Purcell–Meiboom–Gill (CPMG) decoupling sequence with $\tau = 104$ μs. The initialization and readout times were both 5 μs. The image was
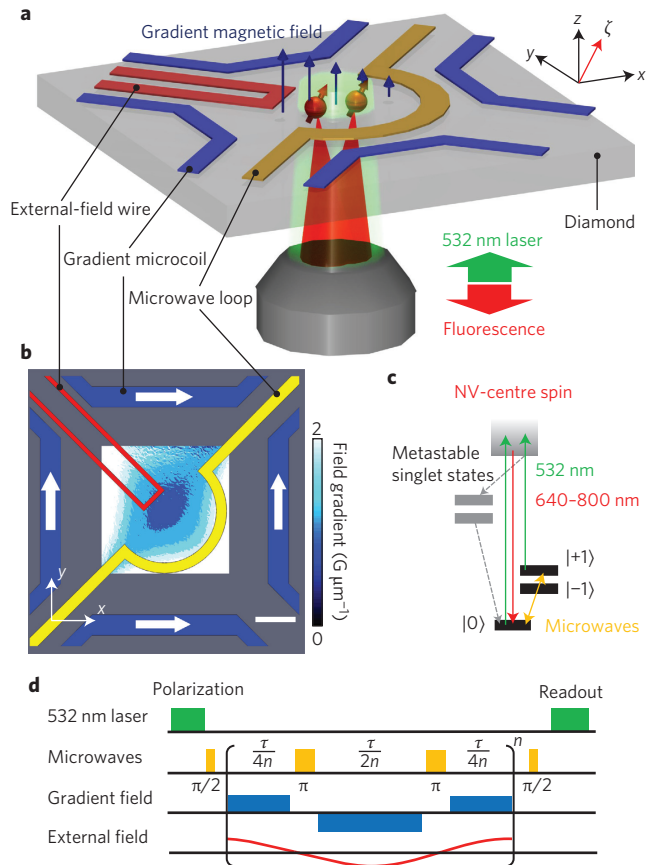
Figure 1 | Fourier magnetic imaging experiment. a, Schematic of the Fourier magnetic imaging microscope. NV-centre magnetic sensors are located near the surface of a diamond chip (for example, as represented by spheres with arrows). NV spin states are initialized and read out with a green (532 nm) laser and coherently manipulated with resonant pulses using a microwave loop. Controlled magnetic field gradients for NV spin phase encoding are generated by sending currents through pairs of gold wires (gradient microcoils) separated by 100 μm and connected in an anti-Helmholtz configuration. An external-field wire is used to create a non-uniform d.c. or a.c. magnetic field for demonstrations of nanoscale Fourier magnetic imaging. The NV quantization axis, represented by ζ, is offset from the surface normal (z-axis) of the [100]-cut diamond sample and aligned with a static, uniform magnetic field of ~30 G created by a permanent magnet (not shown). **b,** Top-view schematic of the Fourier magnetic imaging microscope, as well as a simulation (using COMSOL Multiphysics) of the magnetic field gradient $\sqrt{(dB_\zeta/dx)^2 + (dB_\zeta/dy)^2}$ when a current of 1 A is sent through both microcoil pairs, with current directions indicated by white arrows. Scale bar, 20 μm. **c,** Energy-level diagram of the NV centre (see Methods for details). **d,** Fourier magnetic imaging experimental sequence. Spins are polarized into the $|0\rangle$ state with a green laser pulse. A microwave pulse sequence with $2n$ π pulses dynamically decouples NV centres from magnetic field noise from the environment. A pulsed magnetic field gradient of alternating direction is applied during each precession interval. Spins at different locations accumulate phase at different rates. A final π/2 pulse projects the spins into the $|0\rangle$–$|1\rangle$ manifold, and state populations are read out optically via spin-dependent fluorescence. An a.c. magnetic field B_{ext} produced by current in the external-field wire can be sensed using the procedure described in the main text.

acquired for k values between 0 and 0.144 nm^{-1} in $N_{pix} = 2{,}400$ steps. The sequence was repeated 30,000 times and the total data acquisition time per k value was $T = 3.42$ s. We observed oscillations with a period of 0.0025 nm^{-1} in the k-space image (Fig. 2a). Upon Fourier transformation, the k-space image produced a real-space
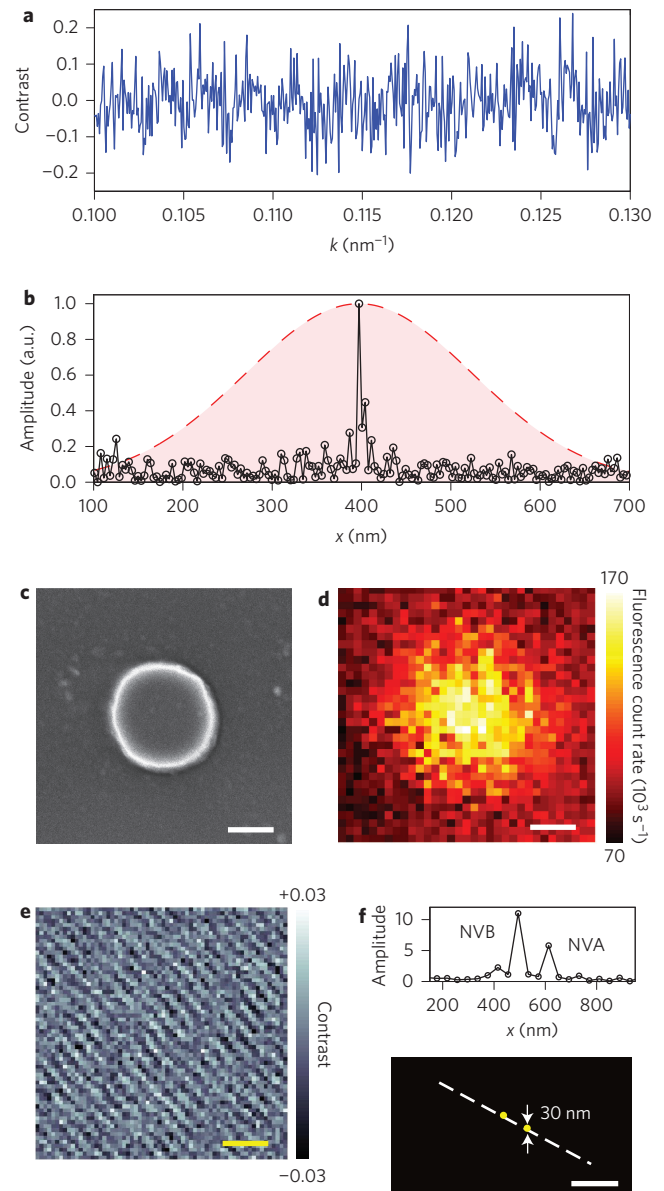

Figure 2 | Fourier imaging of NV centres with nanoscale resolution. a, One-dimensional k-space image of a single NV centre in diamond (sample A) using a four-pulse CPMG sequence ($n = 2$). As the gradient strength dB_ζ/dx is incrementally stepped by varying the current through the microcoil, the NV fluorescence shows sinusoidal oscillations. Here, we show NV fluorescence normalized to a reference measurement of $|0\rangle$ state fluorescence and with a constant background level subtracted. **b,** One-dimensional real-space image data (black) obtained from the absolute value of the Fourier transform of the k-space data. For comparison, the diffraction-limited, real-space point spread function of the microscope is shown (pink shaded area, full-width at half-maximum of 300 nm). **c,** Scanning electron micrograph of a 400-nm-diameter NV-containing diamond nanopillar fabricated on sample B. **d,** Scanning confocal fluorescence image of the same nanopillar (full-width at half-maxima of corresponding x and y profiles of ~400 nm). **e,** Two-dimensional k-space image of two proximal NV centres inside this same nanopillar using a Hahn-echo sequence ($n = 1/2$). **f,** Bottom: Fourier-transformed, two-dimensional real-space image (absolute value) with a threshold set at 5σ above the noise level, where σ is the standard deviation of observed optical noise. Top: cross-section of the two peaks along the direction indicated by the white dashed line in the two-dimensional image. Two NV centres separated by 121(9) nm are clearly resolved. Scale bars: 200 nm (**c,d,f**) and 0.0066 nm^{-1} (**e**).
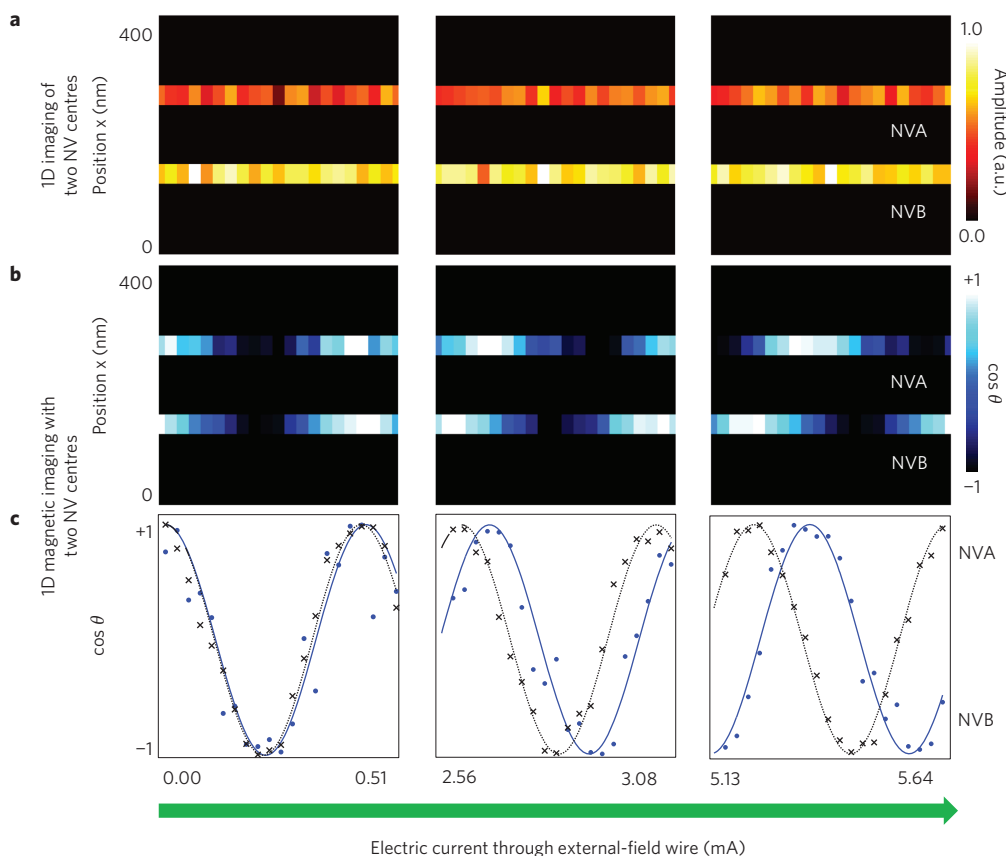
Figure 3 | Fourier magnetic gradient sensing below the optical diffraction limit. One-dimensional k-space magnetic images for the two NV centres shown in Fig. 2f are acquired by incrementally stepping the dB_ζ/dx gradient strength for fixed values of a.c. current sent through the external-field wire. For each current value, the corresponding k-space image is Fourier-transformed and thresholded at 5σ to obtain a one-dimensional real-space image. **a**, Absolute value of the real-space image shows peaks corresponding to the two NV centres separated by 121(9) nm. The vertical axis is real-space position along the x direction and the horizontal axis corresponds to different ranges of a.c. currents at a frequency of 50 kHz, increasing from left to right: 0–0.51, 2.56–3.08 and 5.13–5.64 mA. **b**, Cosine of the argument of the real-space images of the two NV centres shown in **a**, for the same ranges of a.c. currents. **c**, Overlay of measured values for $\cos\theta$ (symbols) and corresponding fits (solids curves) as a function of a.c. current amplitude for the two NV centres, where $\theta = \gamma B_{ext}\tau$. The observed differential phase shift between the data for the two NV centres shows that these spatially separated NV centres measure a magnetic field difference ΔB_{ext} arising from a gradient in the external a.c. magnetic field magnitude B_{ext}.

image with a single peak indicating the single NV location. The peak width and amplitude correspond to a real-space pixel resolution of 3.5(6) nm and SNR = 13 (Fig. 2b). Thus, the data acquisition time to reach SNR = 1 was $T_{SNR=1} = T/SNR^2 \approx 20$ ms. We observed no significant broadening of the real-space signal peak at this image resolution, indicating an insignificant effect from technical issues such as gradient current instability, thermal fluctuations, mechanical vibrations and laser instability.

We next demonstrated two-dimensional Fourier imaging of multiple NV centres using a sample with high NV density (sample B, see Methods). To create a regular pattern of NV centres to be imaged for this and later demonstrations, we fabricated arrays of nanopillars (400 nm diameter, 100 nm height, 1 µm spacing) on the diamond surface. We chose the implant dosage and nanopillar size such that there were, on average, two NV centres of the same crystallographic orientation per nanopillar. Scanning electron microscope and confocal microscope images of a typical nanopillar are shown in Fig. 2c and d, respectively. We used a spin-echo sequence and varied both the dB_ζ/dx and dB_ζ/dy gradient strengths to acquire a two-dimensional k-space image of the NV centres in this nanopillar (Fig. 2e). A Fourier transform of the k-space image, thresholded at 5σ above the noise level (see Supplementary Section V), reveals two proximal NV centres separated by 121(9) nm with a pixel resolution of 30 nm (Fig. 2f). This resolution is consistent with the k-space

spanned in Fig. 2e. For this two-dimensional Fourier image, the data acquisition time to reach SNR = 1 was $T_{SNR=1} \approx 20$ ms.

Once the locations of individual NV centres are determined precisely, they can be used as high-sensitivity probes of magnetic fields that vary on length scales smaller than the optical diffraction limit. To demonstrate such nanoscale Fourier magnetic imaging, we introduced a spatially inhomogeneous magnetic field over the FOV in the centre of the gradient microcoils by sending an alternating electric current, phase-locked to the dynamical-decoupling microwave pulse sequence (Fig. 1d), through the external-field wire shown in Fig. 1a,b. NV centres within this region were thus exposed to different a.c. magnetic field amplitudes depending on their locations relative to the external-field wire. For a fixed value of alternating current, the k-space signal for a given NV at location $\mathbf{r}_0$ acquires a phase offset $\theta = \gamma B_{ext}\tau$, where B_{ext} is the a.c. magnetic field amplitude (projected along the NV axis) at the site of the NV: that is, $s(\mathbf{k}) \sim \cos(2\pi\mathbf{k}\cdot\mathbf{r}_0 + \theta)$. As before, Fourier transforming the k-space image produces a real-space image with abs $[S(\mathbf{r})]$ showing a peak at $\mathbf{r} = \mathbf{r}_0$. Additionally, the argument arg $[S(\mathbf{r}_0)]$ yields the phase shift θ from which B_{ext} can be determined. Figure 3 shows how measured values for B_{ext} can be uniquely assigned to the two NV centres shown in Fig. 2f. For each value of applied alternating current we recorded a one-dimensional k-space image by incrementally varying the dB_ζ/dx gradient strength. Figure 3a shows the
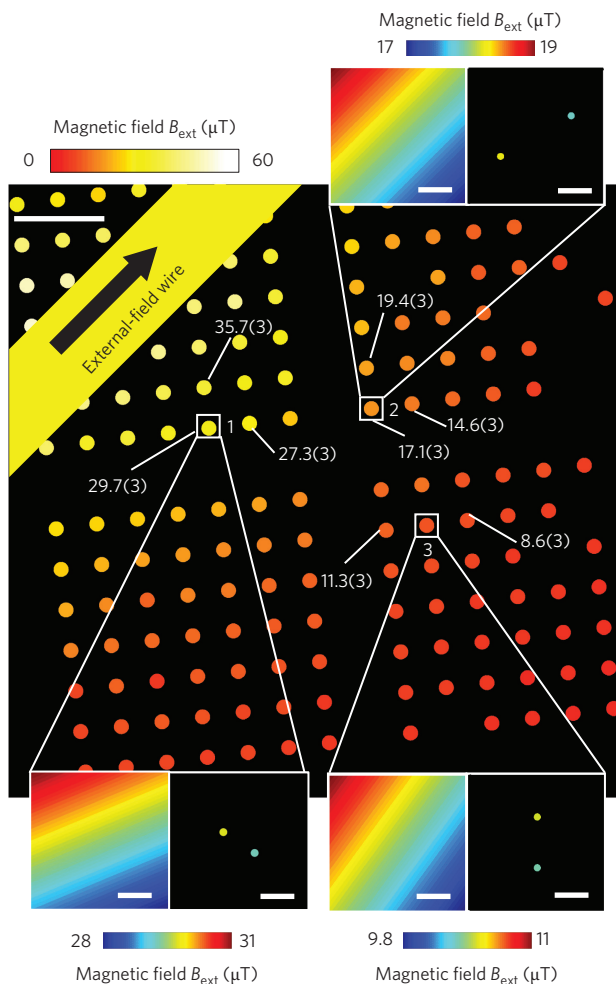
Figure 4 | Fourier magnetic imaging with wide FOV and nanometre-scale resolution. The a.c. magnetic field produced by passing a 50 kHz, 5.13 mA electric current through the external-field wire (indicated by a thick yellow line at the top-left corner) is imaged using a hybrid real + k-space technique over a wide FOV spanning 167 diamond nanopillars. Imaged magnetic field amplitudes are indicated with a colour scale, with numerical values (and associated uncertainties) given for some example nanopillars. A low-resolution real-space magnetic image is acquired over the full FOV by scanning the microscope across all nanopillars (see Methods). The spatial resolution is limited by optical diffraction and NV centres within individual nanopillars are not resolved. Fourier (k-space) magnetic imaging is then performed on individual nanopillars to determine NV centre positions and local a.c. magnetic field amplitudes with ∼30 nm resolution (right boxes of inset panels). To check for consistency, the measured long-range magnetic field gradient provided by the low-resolution real-space image, together with the NV positions determined via Fourier imaging, are used to estimate the variation in a.c. magnetic field amplitude within each nanopillar (left boxes of inset panels). Good agreement is found between the measured and estimated values for the magnetic field difference between NV centres within each nanopillar (Supplementary Section IV). Scale bars: 2 μm (main figure) and 100 nm (insets).

resulting values of $\text{abs}[S(x)]$ as a function of current through the external-field wire with a threshold set at 5σ. We consistently observe two distinct peaks (corresponding to the two NV locations) through the entire current range. The cosine of $\arg[S(x_i)]$, where $x_{i=1,2}$ denotes the location of each peak, is shown in Fig. 3b,c. When the applied current is small (that is, weak B_{ext} gradient), the two NV centres are exposed to nearly the same value

of B_{ext} and consequently there is little difference in the measured NV k-space phases (left panel of Fig. 3c). However, for a larger current of 5.13 mA (that is, stronger B_{ext} gradient, right panel of Fig. 3c), the measured NV k-space phase difference is $2\pi \times (2.6 \pm 0.4) \times 10^{-1}$ rad, which yields a magnetic field difference of $\Delta B_{\text{ext}} = (6.5 \pm 1.1) \times 10^2$ nT between these two NV centres separated by 121(9) nm, equivalent to a magnetic gradient sensitivity of ~ 14 nT nm^{-1} Hz$^{-1/2}$ (Supplementary Section VII). The measured field and gradient values are consistent with those expected from simulations.

NV-diamond Fourier magnetic imaging can also be integrated with wide-field, real-space microscopy to realize a large spatial dynamic range: that is, magnetic imaging with both wide FOV and nanoscale resolution. As a demonstration of such hybrid real + k-space imaging, we scanned the Fourier magnetic microscope across a wide array of NV-containing nanopillars in sample B and performed both low-resolution real-space and high-resolution k-space NV imaging of magnetic field patterns produced by the external-field wire. Real-space image resolution is limited by optical diffraction, while nanometre-scale information is obtained via Fourier magnetic imaging. For example, we sent an alternating current of 5.13 mA and 50 kHz through the external-field wire and performed low-resolution real-space magnetic imaging on 167 nanopillars across 15×15 μm^2 near the edge of the wire (Fig. 4), from which we estimated the magnitude of the magnetic field gradient at each nanopillar location. We next performed high-resolution k-space imaging (followed by Fourier transforming into real space) of both the location of individual NV centres in several nanopillars with 30 nm spatial resolution, as well as the magnetic field difference ΔB_{ext} sensed by the NV centres within each nanopillar. As shown in Fig. 4, the resulting nanoscale maps of ΔB_{ext} are consistent with the local magnetic field gradient values obtained with low-resolution real-space imaging. Together, this hybrid real + k-space imaging demonstration provides a spatial dynamic range (FOV/resolution) of ∼500. In future work we plan to integrate NV Fourier magnetic imaging with a wide-field real-space imager (for example, using a CMOS or charge-coupled device (CCD) camera)[10,14–16], which would obviate the need for scanning and provide parallel and hence rapid real-space imaging across a wider FOV of >1 mm (ref. 27), together with nanoscale-resolution k-space imaging.

Finally, we have shown that the speed of NV Fourier magnetic imaging can be greatly enhanced by compressed sensing[23,24]. We first acquired a fully sampled ($N = 2{,}048$ data points), one-dimensional, k-space image of two NV centres in sample B by sweeping the gradient (blue trace of Fig. 5a). In subsequent measurements we recorded data at $M = N/2^p$ ($p = 0,…,6$) randomly chosen k-space values, providing an N/M-fold speed-up (under-sampling) in data acquisition. For example, the red dots in Fig. 5a show data collected for $M = 128$ k-space values and hence a speed-up of $N/M = 16$. A Fourier transform of the fully sampled curve shows two NV centres separated by 116(4) nm (blue trace in Fig. 5b). The red traces in Fig. 5b show the absolute values of real-space signals reconstructed from the under-sampled data using the l_1-minimization algorithm (see Methods). For $M \geq 128$ we observe two peaks that match well with the NV locations given by the fully sampled data. This result is consistent with the criterion for faithful signal recovery: that is, $M \geq CS \log_2(N)$, where S is the signal sparsity (equal to 2 in the example above) and C is a constant of order 1, which in this case is found to be ∼5. For our experiments $CS \log_2(N) \approx 110$ and thus the signal was not recovered with high probability for $M < 128$. Importantly, we also demonstrated that the reconstructed real-space signal retains information about the magnetic field sensed by each NV centre. We sent an alternating current of 10.26 mA and 50 kHz through the external-field wire, recorded k-space data for $M = 128$ points, and reconstructed
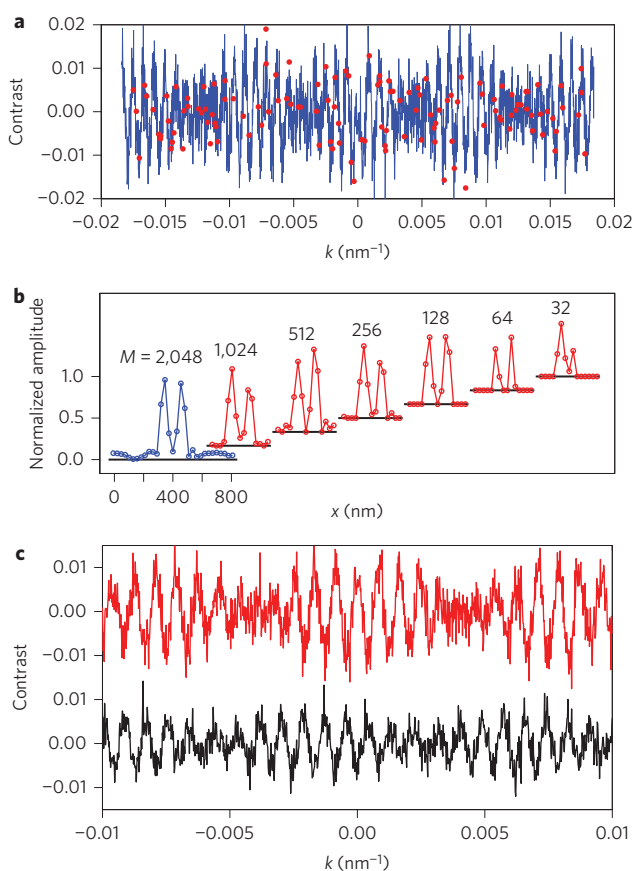
Figure 5 | Compressed sensing speed-up of NV Fourier magnetic imaging.
a, For two NV centres in sample B: fully sampled one-dimensional k-space signal with $N = 2{,}048$ data points (blue line) and randomly under-sampled k-space signal with $M = 128$ data points (red symbols). The under-sampling (speed-up) factor is $N/M = 16$. **b**, Blue trace: absolute value of the Fourier transform of fully sampled k-space data, indicating a real-space NV separation of 116 nm along the x axis. Red traces (offset for clarity): real-space signals reconstructed from under-sampled k-space data sets via compressed sensing techniques, in good agreement with fully sampled k-space data for $M \geq 128$ (see text for details). **c**, Inverse Fourier transform of data reconstructed via compressed sensing for $M = 128$ with (black trace) and without (red trace) an a.c. current (50 kHz, 10.26 mA) sent through an external-field wire. The observed phase shift between the data sets provides a measure of the magnetic field difference between the positions of the two NV centres, in good agreement with the results from fully sampled k-space data, thereby showing that compressed sensing reconstruction retains reliable information about imaged magnetic fields.

real-space signals as described above. From the phase of the reconstructed signals we determined the difference between the magnetic fields sensed by the two NV centres to be $(5.0 \pm 0.5) \times 10^2$ nT, in reasonable agreement with the value of $(6.3 \pm 0.8) \times 10^2$ nT obtained using fully-sampled k-space data, but with the benefit of 16-fold speed-up. The retention of NV phase information in data reconstructed by means of compressed sensing can be made explicit by computing the inverse Fourier transform of the reconstructed signal. In Fig. 5c we compare k-space signals obtained via such inverse Fourier transformations with (black trace) and without (red trace) current in the external-field wire. The observed phase shift between the two traces provides a direct illustration and measure of the magnetic field difference between the two NV centres, consistent with the above results.

Our demonstration of Fourier magnetic imaging provides the first method for mapping NV positions and local magnetic fields

in wavenumber or 'k-space', which is then Fourier-transformed to yield real-space images with both nanoscale resolution and wide FOV. The distinct advantage of this approach relative to real-space imaging is the spatially multiplexed signal acquisition across the full FOV, which enhances the SNR for typical NV centre densities, enables a higher data acquisition rate that can be increased by more than an order of magnitude with compressed sensing, and allows one to probe classical or quantum correlations in samples by conducting simultaneous measurements using multiple, spatially separated NV centres. We also emphasize the relative simplicity of the apparatus needed for Fourier imaging, with the gradient microcoils used for phase-encoding being easily integrated with an optical microscope. We expect that NV Fourier magnetic imaging, which employs phase-encoding of the NV detector spins rather than of the sample spins as in previous Fourier techniques[22], will be applicable to a broad range of systems that can be placed on or near the diamond surface. Example applications in the physical sciences include probing quantum effects in advanced materials, such as frustrated magnetic systems with skyrmionic ordering; spin liquids where quantum spin fluctuations prevent the system from ordering; low-dimensional systems such as graphene, as well as antiferromagnetic and multiferroic materials and topological insulators with quantized spin-carrying surface states. In the life sciences, NV Fourier magnetic imaging may allow nanoscale NMR spectroscopy[28] and structure determination of individual biomolecules, MRI within living cells and real-time, non-invasive mapping of functional activity in neuronal networks with synapse-scale resolution ($\sim$10 nm) and circuit-scale FOV ($>$1 mm). Anticipated technical improvements of NV Fourier imaging include (1) enhanced magnetic field sensitivity via optimization of diamond samples[29], optical collection efficiency[30] and spin-state optical contrast; (2) a 30-fold increase in the k_{max} value, by stronger magnetic field gradients generated by smaller microcoils and larger current and the use of dynamical-decoupling pulse sequences to extend NV spin coherence times[26,31,32]; and (3) parallel real-space image acquisition with a wide-field CMOS or CCD camera, which will provide immediate improvement in the spatial dynamic range (FOV/resolution) and enable the study of long-range, real-time dynamics such as neuronal activity that span length scales from a few nanometres to millimetres. Although instrumentation instabilities such as thermal fluctuations may pose technical challenges, we expect that sub-1 nm resolution is feasible. Straightforward extensions of the present technique should also allow NV Fourier imaging of electric fields[33], temperature[34] and pressure (J. Barry et al., manuscript in preparation) with nanoscale resolution, wide FOV and compressed sensing speed-up, as well as application to other solid-state quantum spin systems such as point defects in silicon carbide[35].

Methods

Methods and any associated references are available in the online version of the paper.

References

1. Taylor, J. M. *et al.* High-sensitivity diamond magnetometer with nanoscale resolution. *Nature Phys.* **4,** 810–816 (2008).
2. Maze, J. R. *et al.* Nanoscale magnetic sensing with an individual electronic spin in diamond. *Nature* **455,** 644–647 (2008).
3. Balasubramanian, G. *et al.* Nanoscale imaging magnetometry with diamond spins under ambient conditions. *Nature* **455,** 648–651 (2008).
4. Grinolds, M. S. *et al.* Nanoscale magnetic imaging of a single electron spin under ambient conditions. *Nature Phys.* **9,** 215–219 (2013).
5. Grinolds, M. S. *et al.* Sub-nanometer resolution in three-dimensional magnetic resonance imaging of individual dark spins. *Nature Nanotech.* **9,** 279–284 (2014).
6. Rondin, L. *et al.* Stray-field imaging of magnetic vortices with a single diamond spin. *Nature Commun.* **4,** 2279 (2013).

7. Mamin, H. J. *et al*. Nanoscale nuclear magnetic resonance with a nitrogen-vacancy spin sensor. *Science* **339,** 557–560 (2013).
8. Staudacher, T. *et al*. Nuclear magnetic resonance spectroscopy on a (5-nanometer)³ sample volume. *Science* **339,** 561–563 (2013).
9. Sushkov, A. O. *et al*. Magnetic resonance detection of individual proton spins using quantum reporters. *Phys. Rev. Lett.* **113,** 197601 (2014).
10. Fu, R. R. *et al*. Solar nebula magnetic fields recorded in the Semarkona meteorite. *Science* **346,** 1089–1092 (2014).
11. Sushkov, A. O. *et al*. All-optical sensing of a single-molecule electron spin. *Nano Lett.* **14,** 6443–6448 (2014).
12. Luan, L. *et al*. Decoherence imaging of spin ensembles using a scanning single-electron spin in diamond. *Sci. Rep.* **5,** 8119 (2015).
13. van der Sar, T. *et al*. Nanometre-scale probing of spin waves using single-electron spins. *Nature Commun.* **6,** 7886 (2015).
14. Le Sage, D. *et al*. Optical magnetic imaging of living cells. *Nature* **496,** 486–489 (2013).
15. Rahn-Lee, L. *et al*. A genetic strategy for probing the functional diversity of magnetosome formation. *PLoS Genet.* **11,** e1004811 (2015).
16. Pham, L. M. *et al*. Magnetic field imaging with nitrogen-vacancy ensembles. *New J. Phys.* **13,** 045021 (2011).
17. Maletinsky, P. *et al*. A robust scanning diamond sensor for nanoscale imaging with single nitrogen-vacancy centres. *Nature Nanotech.* **7,** 320–324 (2012).
18. Maurer, P. C. *et al*. Far-field optical imaging and manipulation of individual spins with nanoscale resolution. *Nature Phys.* **6,** 912–918 (2010).
19. Wildanger, D. *et al*. Solid immersion facilitates fluorescence microscopy with nanometer resolution and sub-ångström emitter localization. *Adv. Mater.* **24,** OP309–OP313 (2012).
20. Sodickson, A. & Cory, D. G. A generalized *k*-space formalism for treating the spatial aspects of a variety of NMR experiments. *Prog. Nucl. Magn. Reson. Spectrosc.* **33,** 77–108 (1998).
21. Ernst, R. R. & Anderson, W. A. Application of Fourier transform spectroscopy to magnetic resonance. *Rev. Sci. Instrum.* **37,** 93–102 (1966).
22. Nichol, J. M. *et al*. Nanoscale Fourier-transform magnetic resonance imaging. *Phys. Rev. X* **3,** 031016 (2013).
23. Candès, E., Romberg, J. & Tao, T. Robust uncertainty principles: exact signal reconstruction from highly incomplete frequency information. *IEEE Trans. Inf. Theory* **52,** 489–509 (2006).
24. Lustig, M., Donoho, D. L., Santos, J. M. & Pauly, J. M. Compressed sensing MRI. *Signal Process. Mag. IEEE* **25,** 72–82 (2008).
25. De Lange, G., Wang, Z. H., Ristè, D., Dobrovitski, V. V. & Hanson, R. Universal dynamical decoupling of a single solid-state spin from a spin bath. *Science* **330,** 60–63 (2010).
26. Pham, L. M. *et al*. Enhanced solid-state multispin metrology using dynamical decoupling. *Phys. Rev. B* **86,** 045214 (2012).
27. Glenn, D. R. *et al*. Single-cell magnetic imaging using a quantum diamond microscope. *Nature Methods* **12,** 736–738 (2015).
28. DeVience, S. J. *et al*. Nanoscale NMR spectroscopy and imaging of multiple nuclear species. *Nature Nanotech.* **10,** 129–134 (2015).
29. Pham, L. M. *et al*. Enhanced metrology using preferential orientation of nitrogen-vacancy centers in diamond. *Phys. Rev. B* **86,** 121202(R) (2012).
30. Le Sage, D. *et al*. Efficient photon detection from color centers in a diamond optical waveguide. *Phys. Rev. B* **85,** 121202(R) (2012).
31. Bar-Gill, N. *et al*. Suppression of spin-bath dynamics for improved coherence of multi-spin-qubit systems. *Nature Commun.* **3,** 858 (2012).
32. Bar-Gill, N., Pham, L. M., Jarmola, A., Budker, D. & Walsworth, R. L. Solid-state electronic spin coherence time approaching one second. *Nature Commun.* **4,** 1743 (2013).
33. Dolde, F. *et al*. Electric-field sensing using single diamond spins. *Nature Phys.* **7,** 459–463 (2011).
34. Kucsko, G. *et al*. Nanometre-scale thermometry in a living cell. *Nature* **500,** 54–58 (2013).
35. Koehl, W. F., Buckley, B. B., Heremans, F. J., Calusine, G. & Awschalom, D. D. Room temperature coherent control of defect spin qubits in silicon carbide. *Nature* **479,** 84–87 (2011).

Author contributions
K.A., C.B and H.Z. contributed equally to this work. R.L.W. conceived the idea of NV Fourier magnetic imaging and supervised the project. K.A., C.B. and H.Z. developed measurement protocols, hardware and software for NV Fourier magnetic imaging, performed the measurements and analysed the data. C.B. and N.B.-G. developed the NV-diamond confocal microscope used in the study. N.B.-G. also aided the development of data acquisition software. S.J.D. and A.Y. advised on Fourier imaging techniques and applications. P.C. advised on compressed sensing techniques and applications. All authors discussed the results and participated in writing the manuscript.

Additional information
Supplementary information is available in the online version of the paper. Reprints and permissions information is available online at www.nature.com/reprints. Correspondence and requests for materials should be addressed to R.L.W.

Competing financial interests
The authors declare no competing financial interests.

Methods

NV physics. The ground state of the NV centre is a spin-triplet with a 2.87 GHz zero-field splitting between the $|0\rangle$ and $|\pm1\rangle$ spin states (Fig. 1c). An applied magnetic field defines a quantization axis and Zeeman splits the $|\pm1\rangle$ states. Under optical excitation at 532 nm, the NV centre undergoes spin-state-preserving transitions between the electronic ground and excited states, emitting fluorescence in the 640–800 nm band. A non-radiative decay pathway from the $|\pm1\rangle$ excited states to the $|0\rangle$ ground state allows optical initialization of the NV centre, as well as optical readout of the spin state via the spin-state-dependent fluorescence intensity.

Fabrication of nanopillars and gradient microcoils. Samples A and B were electronic-grade, single-crystal diamond chips with natural isotopic concentration of ^{13}C (1.1%), which were grown using chemical vapour deposition (Element 6 Corporation). Sample A was implanted with ^{14}N ions (dosage, 1×10^{10} cm^{-2}; energy, 85 keV). From the stopping and range of ions in matter simulations, the NV centres were estimated to be 100 nm below the diamond surface. Sample B was implanted with ^{15}N ions (dosage, 1×10^{12} cm^{-2}; energy, 14 keV) and the estimated NV depth was 20 nm. The conversion efficiency from implanted N ions to NV centres in both samples was estimated to be ~1%. Typical NV spin dephasing times were $T_2^* \approx 1$ μs (sample A) and 500 ns (sample B), and the typical Hahn-echo spin coherence times were $T_2 \approx 50$ μs (sample A) and 30 μs (sample B). The magnetic field gradients used in the Fourier imaging demonstrations did not significantly affect NV spin coherence properties across the imaging FOV[36]. To fabricate diamond nanopillars, sample B was spin-coated with a 100-nm-thick layer of electron-beam resist (Dow Corning, XR-1541-006). Arrays of 400-nm-diameter circles were then patterned using an Elionix ELS-7000 electron-beam writing system with exposure dosage and beam energy set at 8,000 μC cm^{-2} and 100 kV, respectively. Tetra-methyl ammonium hydroxide (25%) was used to develop the resist and form the etch mask. The diamond crystal was then placed in an inductively coupled plasma (ICP) reactive-ion etching system and etched for 45 s with 30 s.c.c.m. of oxygen gas, 700 W ICP power and 100 W bias power at a chamber pressure of 10 mtorr. These parameters gave an etch depth of ~150 nm. The gradient microcoils, microwave loop and external-field wire were fabricated on a polycrystalline diamond coverslip ($10 \times 10 \times 0.3$ mm^3) for optimized heat dissipation. The coverslip was spin-coated with LOR 20B (MicroChem, bottom layer, ~2 μm) and Shipley S1805 (Dow Electronic Materials, top layer, ~400 nm) photoresists, exposed using a mask aligner, and the pattern was developed in a CD26 bath. A 30 nm Ti layer and a 970 nm Au layer were then deposited in an electron-beam evaporator, followed by lift-off in MicroChem Remover PG solution. Electrical resistance measurements, performed using a four-probe station, gave a value of ~1 Ω for each gradient microcoil. The diamond coverslip was bonded to the NV-containing diamond sample with optical adhesive, and a copper heat sink was attached to the back surface of the diamond coverslip to enhance heat dissipation.

Data analysis. Fourier magnetic imaging signals were recorded in k-space using the techniques described in the main text. A tapered-cosine windowing function with the taper coefficient set to 0.1 was applied to the k-space data and a symmetric fast Fourier transform algorithm implemented with MATLAB was used to obtain real-space images. No zero padding was done on the k-space data. Real-space pixel resolution therefore matched the true resolution of the imaging system. The SNR of real-space images acquired with this method increased with the square root of the number of data points, confirming the multiplex advantage of the Fourier imaging technique (Supplementary Section VI). The real-space images in Figs 2, 3 and 4 were thresholded at 5σ above the noise level (where σ is the standard deviation of the noise) and NV centres were represented by circles centred at the positions of the thresholded peaks, with diameters equal to the pixel resolution. For the wide FOV image of Fig. 4, the k-space sampling rate and number of sample points were held fixed for all nanopillars. For the magnetic field sensing data of Fig. 4, a calibration procedure was first performed by recording NV fluorescence as a function of current through the external-field wire for each nanopillar in the FOV without phase encoding. The resultant magnetometry curves revealed the functional dependence of the magnetic field on the applied current for each nanopillar. For a fixed current, the magnetic field so determined was used as an offset value for the high-spatial-resolution phase-encoded magnetic field data recorded from individual NV centres within the nanopillar of interest. Magnetic field sensitivity was calculated as $(\sigma_B/dS_B)T^{1/2}$, where σ_B is the measurement noise, dS_B is the slope of the magnetometry curve, and T is the total data acquisition time. For the NV centres and measurement protocols employed in this work, the magnetic field sensitivity was ~1 μT Hz$^{-1/2}$.

Compressed sensing. In compressed sensing, signals are sampled at random and at a sampling frequency that may be lower than the Nyquist rate. Under assumptions of signal sparsity, recovery algorithms based on convex optimization can then be used to reconstruct the signal in a transform domain with high fidelity. In the present compressed sensing demonstration, the under-sampled k-space data were windowed with a tapered-cosine function (taper parameter of 1). A Fourier transform sampling matrix A of size $M \times N$ was created by picking M rows (corresponding to the sampled points) from an $N \times N$ discrete Fourier transform matrix. The real-space signal was reconstructed from the under-sampled data sets by minimizing the l_1-norm of the real-space signal $||\mathbf{x}_1||$ subject to the constraint $\mathbf{k} = A \cdot \mathbf{x}$, where $\mathbf{x}$ and $\mathbf{k}$ are column vectors of size N and M representing real-space and k-space data respectively. The convex optimization routine was implemented using MATLAB library functions made available by CVX Research (www.cvxr.com).

References

36. Stanwix, P. L. *et al.* Coherence of nitrogen-vacancy electronic spin ensembles in diamond. *Phys. Rev. B* **82**, 201201(R) (2010).